Elastodynamic erosion of thermal barrier coatings

Man Wang, Norman A. Fleck* and Anthony G. Evans**

Cambridge University, Department of Engineering,

Trumpington Street, Cambridge, CB2 1PZ, UK

Abstract

The finite element method is used to analyse the elastodynamic response of a columnar thermal barrier coating due to normal impact and oblique impact by an erosive particle. An assessment is made of the erosion by crack growth from pre-existing flaws at the edge of each column: it is demonstrated that particle impacts can be sufficiently severe to give rise to columnar cracking. First, the transient stress state induced by normal impact of a circular cylinder or a sphere is calculated in order to assess whether a 2D calculation adequately captures the more realistic 3D behaviour. It is found that the transient stress state for the plane strain and axisymmetric models are similar. The sensitivity of response to particle diameter and to impact velocity is determined for both the cylinder and sphere. Second, the transient stress state is explored for 2D oblique impact by a circular cylindrical particle and by an angular cylindrical particle. The sensitivity of transient tensile stress within the columns to particle shape (circular and angular), impact angle, impact location, orientation of the angular particle and to the level of friction are explored in turn. The paper concludes with an evaluation of the effect of inclining the TBC columns upon their erosion resistance.

Keywords: Thermal barrier coatings, finite element analysis, erosion, elastodynamic loading

*Corresponding author. Tel.:+44 1223 748240: fax: +44 1223 765046

E-mail address: naf1@eng.cam.ac.uk

** This research was initiated when Prof. Evans was on sabbatical from University of California, Santa Barbara at Cambridge University. The two other authors are indebted to him for his contributions to his article, and for his wise counsel and friendship over the years.

1. Introduction

Thermal barrier coatings (TBCs) are widely used in gas turbines for aerospace propulsion and power generation. The current coating system consists of three layers [1]. The outer layer is the thermal barrier (TB) against hot combustion gases, and typically comprises yttria-stabilized zirconia (YSZ). Oxidation resistance is achieved by an underlying thermally grown oxide (TGO) layer of alumina. The TGO progressively thickens during service by the oxidation of an underlying aluminium-rich bond coat. Two distinct topologies of TB layer exist. One comprises layers of splats deposited by an air plasma spray technique (APS), and the other consists of a columnar microstructure produced by electron beam physical vapor deposition (EB-PVD). There is continued development on the topology of EB-PVD coatings in order to optimise their thermal barrier properties, ideally without loss of durability. For example, inclined TBC columns have increased thermal resistance [2, 3] but the recent experimental evidence of Nicholls [4-6] reveals that they have a reduced resistance to erosion. In this paper we limit attention to the erosion of columnar TBCs made by the EB-PVD route and explore the sensitivity of elastodynamic response (and thereby the anticipated erosion response) to the topology of coating, level of contact friction, size and shape of impacting particle, and to the angle and site of impact of the incoming particle.

Two distinct erosion mechanisms have been identified for EB-PVD TBCs [7]. One involves plastic indentation and the other is elastodynamic in nature. The plastic damage, including plastic densification and microbuckling of the columnar TBCs, accompanies impact by large particles with high momentum and at high temperature.

The deformation zones develop over a millisecond timescale, as the impacting particle decelerates [8].

In contrast, elastodynamic failure is caused by the impact of small particles of low momentum and at low temperature. Elastic waves emanate from the contact and lead to trans-columnar cracks beneath the surface. Zisis and Fleck [9, 10] have studied the elastodynamic response of the columns to normal impact by a spherical particle using the finite element method. The columns act as wave-guides, and the transient tensile stress generated by the impact event is sufficient to crack the columns. Typical stress histories are reported in detail in [8-10] but attention is limited to normal impact by spherical particles at a limited range of speeds. The predicted site of column cracking is in good agreement with experimental observations of [11] : the columns crack at a depth somewhat less than their diameter.

In the practical case of erosion of TBC coatings by foreign particles, there are a number of complicating features that have hitherto been ignored in the idealised finite element calculations. The particles may not be smooth and spherical, they may impinge the TBC at an angle which deviates from the normal direction, and the TBC columns themselves can be inclined. We address the significance of these complicating features in the current study. The focus of this paper is on the elasto-dynamic response of EB-PVD TBCs to normal and oblique impact by a foreign particle. The ABAQUS/Explicit finite element program (Version 6.5) [12] is used to analyse the impact event for both circular and angular erosive particles. The primary objective is to explore the sensitivity of the transient stress state to the wide range of geometric and kinematic variables that define the impact event, including the size of erosive particle, initial velocity of the particle, angle of incidence, impact location at

the top of a TBC column, inclination of the angular particle and the level of Coulomb friction between columns and at the particle-column contact. The transient stress state is used to determine the potential for cracking: the static stress intensity factor is calculated for a putative crack in the columns. Recently, it has been suggested that the thermal resistance of TBC columns is increased by depositing them at an inclination to the normal direction [2, 3]. We end the paper with an assessment of the degree to which this influences the erosion resistance under elastodynamic loading.

A full 3D finite study of a columnar TBC impacted by a 3D particle is prohibitively expensive in computer resources, and so the study focuses on the 2D, plane strain problem of oblique impact of an array of strip-like TBC columns by a cylindrical projectile. To validate this approach, the case of normal impact is considered for both axisymmetric and plane strain cases, and it is demonstrated that the plane strain problem is adequate for capturing the main features of the elastodynamic response of the more realistic axisymmetric case and thereby the full 3D problem.

2. Normal impact of the columnar TBC layer

In order to study the normal impact event, a plane strain finite element model and an axisymmetric finite element model are each established, as sketched in Figs. 1a and 1b, respectively. (The direction of normal impact is defined by $\phi = 0$ in Fig. 1a.) The EB-PVD columns are perfectly bonded to a rigid substrate for both models. In the plane strain model, the columnar TBC layer is represented by a set of vertical aligned rectangular strips, and the foreign particle is represented by a circular cylinder. In contrast, for the axisymmetric model, the TBC layer is simulated by a nested annular

array of circular cylinders, and the particle is a sphere of radius R. A Cartesian reference frame is adopted for both models.

2.1 Material and geometric parameters

The columns in both the plane strain model of Fig. 1a and in the axisymmetric model of Fig. 2a are of width d, height $H_{\mathrm{TBC}}=20d$, and inter-columnar gap $g=0.01d$. A linear elastic response is assumed for the columnar structure with a Young's modulus E_{TBC}, Poisson's ratio ν, and density ρ_{TBC}. The incident particle is taken to be rigid and of density $\rho_{\mathrm{p}}=0.34\rho_{\mathrm{TBC}}$, to represent the relative density values for a silica particle and a YSZ TBC. Its radius ranges from $R=0.5d$ to $R=10d$, and its initial velocity ranges from $V_0=0.01c$ to $V_0=0.3c$. The particle is allowed to decelerate after impact due to the transient contact force exerted upon it by the TBC columns. A reference, 1D elastic wave speed is also introduced as $c=\sqrt{E_{\mathrm{TBC}}/\rho_{\mathrm{TBC}}}$, and is used below for normalisation of the impact velocity.

2.2 The finite element simulations

A mesh sensitivity study reveals that the plane strain column model of Fig. 1a achieves adequate accuracy by using 240,697 4-noded quadrilateral plane strain elements (CPE4R in ABAQUS); likewise, the axisymmetric model has adequate accuracy by using 164,126 4-noded quadrilateral axisymmetric elements (CAX4R in ABAQUS).

The displacement boundary conditions for the two models are $u_1=u_2=0$ along the bottom. Additionally, the displacement boundary condition $u_1=0$ is prescribed along the center line in the axisymmetric model. Traction-free side boundaries are assumed. Numerical experiments reveal that axial stress waves in the central column propagates to the substrate in about 50ns after impact; since our study is limited to the initial elastodynamic response near the tops of the columns the total calculation time is limited to 50ns. Thus, the choice of boundary conditions on the side boundary is not significant since the stress waves do not propagate to the sides within 50ns.

Small deformations are assumed in all calculations. Automatic time-stepping is performed with the Courant condition automatically satisfied. The default value of material viscosity in ABAQUS is used throughout. The contact pair algorithm in ABAQUS is chosen to calculate the contact between the incoming particle and the TBC, and the default options of mechanical constraint formulation and sliding formulation are employed. Frictionless conditions are assumed between columns, and between the particle and columns.

2.3 Typical elastodynamic response

Immediately following impact an elastic wavetrain emanates from the contact and travels down the TBC columns, as outlined in [10] for the axisymmetric case. The degree to which the columns behave as independent waveguides or as the elements of a half-space depends upon the column diameter d and gap size g between columns in relation to the radius R of the particle. A typical elastodynamic response for the axisymmetric problem is reported in [10]; here, we summarise the equivalent plane-strain case to show that the response is qualitatively similar to the axisymmetric

response. Snapshots of the transient stress distribution are given in Fig. 2a for normal impact; for later discussion, predictions are shown in Fig. 2b for impact at an angle of $\phi = 45^o$. (The results are given for E_{TBC} =140 GPa, ν=0.3, ρ_{TBC}=5900 kgm^{-3}, d=10 μm, g=0.1 μm, H_{TBC}=20μm, V_0=300 ms^{-1} , R=25 μm, ρ_P=2000 kgm^{-3}, $\mu_C = \mu_S = 0$ in order to allow for a comparison with the axisymmetric results given in Fig. 3 of [10]).

Contours of tensile axial stress σ_{22} are shown, with the colour white indicating axial compression. Immediately following impact a combination of longitudinal, shear and Rayleigh waves emanate from the contact into the central column. After a time t = 1ns a local maximum stress of 1.3 GPa is attained at the side-surface of the central column and at a depth of 1μm below the surface. The central column then comes into contact with the adjacent column, and the ensuing response is similar to that already experienced by the central column. A peak tensile stress of 3.7GPa is attained in both space and time (at t = 6ns), compared with an overall peak value of 3.9GPa for the axisymmetric case reported in [10]. The stress transient travels down the columns as depicted in the snapshot at 8ns and then 15ns. It is clear that the wavetrain from the impact site disperses throughout the TBC coating by the collision of neighbouring columns, leading to a complex and highly non-uniform transient stress state. In addition to the tensile waves shown in Fig. 2a, compression waves travel down the central columns but further consideration of these is discounted here; the present study concerns itself with the more damaging tensile waves near the surface of the coating that lead to surface erosion.

Our main concern is the possibility of cracking at the edge of the columns due to the transient tensile axial stress σ_{22}. Write $(\sigma_{22})_{max}$ as the spatial and temporal maximum

value of tensile stress within the columns over the initial impact period of 50ns. Then, define the normalized maximum tensile stress $\overline{\sigma}_{22}$ as

$$\overline{\sigma}_{22} = \frac{(\sigma_{22})_{\max}}{\sqrt{E_{\mathrm{TBC}}\rho_{\mathrm{TBC}}}V_0} \tag{1}$$

The denominator of equation (1) is a reference tensile stress: it is the uniaxial tensile stress in an elastic rod (made from TBC material) when subjected to a step-wise jump in axial velocity of V_0 at one end [m]. An assessment is now made for the value of $\overline{\sigma}_{22}$ that leads to cracking from the edge of the columns. Then, in the remainder of this section we shall explore the sensitivity of $\overline{\sigma}_{22}$ to the size and initial velocity of the impacting particle for both the plane strain and axisymmetric problems.

Assessment of crack initiation under the transient stress field

It is instructive to assess whether the stress level $\overline{\sigma}_{22}$ from the elastodynamic simulations is sufficiently high to lead to tensile failure from the edge of the feathery TBC columns. Here, we perform a preliminary fracture mechanics assessment and calculate the maximum mode I stress intensity factor for incipient flaws at the edge of each TBC column. The role of material inertia is ignored in the calculation of mode I stress intensity factor from the stress state $\overline{\sigma}_{22}$: it is appreciated that this is only an approximation, but our intent is to provide an overall assessment of whether the elastodynamic stress field is sufficiently intense to lead to erosion of the coating.

Microstructural observations of TBC coatings suggest that the feathery edges of the EB-PVD columns possess crack-like flaws of length *a* on the order of 1μm along the

sides of each column. Further, it is observed from the finite element simulations of the present study that the transient tensile stress distribution occurs to a depth on the order of 1μm from the free edge; this stress state is approximated by a triangular waveform from a maximum value at the edge of the column to zero at the crack tip. Now, the stress intensity factor K_I for an edge crack of length a in a semi-infinite plate, subjected to a linear distribution of traction from σ at the crack mouth to zero at the crack tip, is given by $K_I = 1.208(1-2/\pi)\sigma\sqrt{\pi a}$ [14]. Assume a representative value of fracture toughness of the TBC layer to be K_{IC}=1 MPa$\sqrt{m}$ and, with a=1μm, this gives a critical value of stress σ_C = 1.65 GPa. For an impact velocity V_0=300 ms^{-1}, along with E_{TBC} =140 GPa and ρ_{TBC}=5900 kgm^{-3}, relation (1) implies that the critical value of $\bar{\sigma}_{22}$ is given by $\bar{\sigma}_{22} = \bar{\sigma}_C = 0.19$. We shall show below that the level of peak axial stress $\bar{\sigma}_{22}$ in many of the elastodynamic simulations exceeds this threshold value and consequently crack growth from the edge flaws is anticipated.

2.4 The effect of particle size and initial impact velocity upon the transient tensile stress

The FE simulations reveal that the maximum transient tensile stress occurs at the edge of the column and at a depth of 0.2-2.2d. The non-dimensional peak stress $\bar{\sigma}_{22}$ is evaluated for selected values of V_0/c and is plotted as a function of d/R in Fig. 3a for the plane strain problem, and in Fig. 3b for the axisymmetric case. For both problems, $\bar{\sigma}_{22}$ decreases somewhat with increasing d/R. The mild but non-monotonic dependence of $\bar{\sigma}_{22}$ upon V_0/c is associated with the details of contact evolution between columns. In broad terms, the plane strain model adequately mimics the

elastodynamic response of the axisymmetric model but predicts somewhat higher stress levels. For both types of model, the impacting particle has retarded to a minor degree (5%-20% depending upon the value of d/R) over the time interval for the attainment of maximum tensile stress. An analytical model for the deceleration of the particle has been given by Fleck and Zisis [10], including validation by finite element simulation. They show that the contact pressure exerted by the columnar TBC upon the particle scales with the instantaneous particle velocity V according to

$$p = V\sqrt{E_{\mathrm{TBC}}\rho_{\mathrm{TBC}}} \qquad (2)$$

The column number n for which the maximum tensile stress occurs, counted from the initial contact point, is plotted against the normalised particle size d/R in Figure 4a for the plane strain model and in Figure 4b for the axisymmetric case. Both models give similar trends: the column that suffers the highest transient stress is located further from the centre line with increasing V_0/c and decreasing d/R. The surprising result that the peak stress is attained in a column several diameters away from the impacted column is a consequence of the highly non-linear contact interactions along with the ensuing complex pattern of wave motion.

3. Oblique impact of the columnar TBC layer

It is of interest to determine the sensitivity of axial stress to the obliquity of impact and to the impact site at the top of the columns. We limit attention to the 2D plane strain case, and assume that the cylindrical particle has an incoming velocity V_0 at an angle ϕ to the normal, and impacts a column at a distance s from its mid-plane, as defined in Fig. 1. The same FE mesh, boundary conditions and time stepping

conditions were used for oblique impact as for normal impact. Again, the maximum value of transient tensile stress along the axis of the columns was determined over the first 50ns required for stress wave propagation to the bottom of the TBC columns.

The impact problem now involves a larger number of geometric parameters. The sensitivity of elasto-dynamic response to the inter-columnar gap size g, and height of column H_{TBC} has been previously addressed [9] for the case of normal impact. Accordingly, in the remainder of this study, values for (g, H_{TBC}) are fixed at g=0.01d and H_{TBC}=20d. We also limit attention to a circular cylinder of radius R=2.5d and of density ρ_{p}=0.34ρ_{TBC}. The particle impinges the underlying TBC at an initial velocity $V_0 = 0.062\sqrt{E_{\mathrm{TBC}} / \rho_{\mathrm{TBC}}}$ and, for the case of a TBC made from YSZ, this corresponds to an impact velocity of the tip of the turbine blades, $V_0 =$ 300 ms^{-1}.

The sensitivity of the maximum axial stress to the impact angle ϕ for three selected values of impact location s=-d/4, 0 and d/4 is given in Fig. 5 for the frictionless case μ_{s}=μ_{c}=0. The peak stress drops by a factor of about four when the angle of obliquity ϕ is increased from 0 to 75$^{\mathrm{o}}$, and increases slightly when the impact site is located off-centre $s \neq 0$. In order to assess whether the peak axial stress is dictated simply by the *vertical* component of particle velocity an additional stress trajectory has been added to Fig. 5, as follows. The normal component of impact velocity is given by $V_o \cos\phi$ and if this velocity component were to dictate the peak stress attained then the peak stress $\bar{\sigma}_{22}$ at an incidence of ϕ would be related to the peak stress $(\bar{\sigma}_{22})_0$ for normal

impact according to $\bar{\sigma}_{22} = (\bar{\sigma}_{22})_0 \cos\phi$. This function is plotted in Fig. 5 for the choice s =0; it is an adequate approximation for $\phi < 15^o$ but underestimates the peak stress by about 20% at large ϕ.

The transient stress history for oblique impact is asymmetrical with respect to the centre line of the column, but is otherwise qualitatively similar. An example of the axial stress distribution at the instant of peak local stress for $s=\mu_s=\mu_c=0$ and $\phi=45^o$ is shown in Fig. 6c. The location of peak stress is almost identical to that for $s=\mu_s=\mu_c=0$ and $\phi=0$, recall Fig. 6a. For completeness, the axial stress distribution at peak local stress is included in Fig. 6 for normal impact $\phi=0$ and inclined impact $\phi=45^o$ with $\mu_s=\mu_c=1$ and $s=0$. This high value of friction coefficients leads to significant changes in the location of peak stress and to a moderate increase in value (by 20% for $\phi=0$, and by 80% for $\phi=45^o$).

3.1 The effect of particle shape upon the transient tensile stress

Foreign object debris is usually angular in shape rather than circular, and it is interest to determine the sensitivity of the elastodynamic response to the details of the particle shape. We consider a prototypical angular particle in the form of a square cylinder of side length a=4.4d with a rounded-off corner of radius r=0.2d, see Fig. 7. The angle of attack ψ of the square particle is also defined in Figure7 ; it has the selected values of $-\pi/8$, 0, $\pi/8$ and $\pi/4$ in our study.

The nondimensional tensile stress $\bar{\sigma}_{22}$ depends upon several factors such as the particle shape, the impact angle ϕ, the friction condition, the initial impact location and the orientation of the angular particle. The sensitivity of $\bar{\sigma}_{22}$ to ϕ is shown in Fig. 8 for the circular and square particles, for (a) $\mu_s=\mu_c=0$ and (b) $\mu_s=\mu_c=1$. Both particles impact the mid-point of the TBC columns, s=0, and the square particle is orientated so that it has zero angle of attack, ψ=0. It is clear from Fig. 8 that the dependence of peak stress $\bar{\sigma}_{22}$ upon the angle of incidence ϕ is sensitive to both particle shape and to the level of friction. The circular particle contacts and bends two underlying columns at the same time, whereas the square particle initially touches and bends the first column by its corner and then bends the second column by its side. Consequently, the stress transients are different. For the circular particle and frictionless contacts, $\bar{\sigma}_{22}$ gradually reduces from 0.41 to 0.14 when ϕ increases from 0° to 75°. With high friction present, $\bar{\sigma}_{22}$ first increases with increasing ϕ and then attains a peak value at ϕ equal to approximately 30^o.

For the square particle and frictionless conditions, $\bar{\sigma}_{22}$ is on the order of 0.3 for ϕ in the range 0° to 45°, then increases rapidly to 0.44 as ϕ is increased to ϕ=60° and then drops to 0.35 at ϕ=75°. The maximum tensile stresses occur at initial 2ns to 3ns and at depth of 2μm at small impact angles (ϕ = 0º-30º). However, at large impact angles (ϕ = 45º-75º), the maximum tensile stresses occur after 30ns to 40ns and at a depth of 30μm to 60μm. An increase in friction level causes $\bar{\sigma}_{22}$ to attain a higher peak value of about 0.85 but at a reduced value of angle of attack, $\phi = 30^o$, see Fig. bb.

In broad terms, $\bar{\sigma}_{22}$ varies over a wide range, from 0.15 to 0.85, depending upon particle shape, friction level and angle of incidence. This is consistent with the

feature that particle erosion of TBC systems is a highly stochastic event: there is a wide variation in impact damage from one particle to the next [6].

3.2 Square particles: the effect of angle of attack and impact location upon stress state

The effect of impact location *s* and angle of attack ψ of the square particle upon the $\bar{\sigma}_{22}$ versus ϕ response is shown in Figure 9, for frictionless contacts. Three initial impact locations are chosen, *s*=0.0, 0.25*d* and -0.25*d* in Fig. 9a, with ψ=0. The initial impact location has a minor effect upon the magnitude of the non-dimensional maximum tensile stress, as for the circular particle, recall Fig. 5. The angle of attack ψ has a more dramatic effect upon $\bar{\sigma}_{22}$, particularly at oblique impacts with ϕ on the order of 60^o, see Fig. 9b For this value of ϕ, $\bar{\sigma}_{22}$ increases from 0.1 to 0.6 as ψ is increased from $-\pi/8$ to $\pi/4$.

4. The elastodynamic response of inclined TBC columns

Inclined TBC columns provide greater thermal insulation than vertical columns, but have a reduced erosion resistance. In this section, the elastodynamic response of inclined columns is compared with that of vertical columns, first for normal impact and then for inclined impact by circular cylindrical particles.

4.1 Normal impact of inclined columns

The impact response has been explored for normal impact (ϕ = 0) of an array of inclined columns, as defined by the angle β in Fig. 10. Otherwise, the geometry and material parameters are the same as those used for the vertical columns as defined above. The rigid particle is a circular cylinder of radius R=2.5d and density ρ_{p}=0.34ρ_{TBC}, and it impacts the underlying columnar coating perpendicularly at an initial velocity $V_0 = 0.062\sqrt{E_{\mathrm{TBC}} / \rho_{\mathrm{TBC}}}$ (corresponding to 300 ms^{-1} in a practical system). For the present calculations, all the contacts are assumed to be frictionless.

The commercial finite element software ABAQUS/Explicit was again employed, with the implementation details and boundary conditions as described in previous sections of this paper. A typical elastodynamic response for columns inclined at β = 60$^{\mathrm{o}}$ is shown in Fig. 11: contours of the tensile stress σ_{a} co-axial with the columns are shown after 2ns and after 8ns. It is instructive to compare the response with that shown in Fig. 2 for normal impact (ϕ = 0) of vertical columns. For the case of inclined columns (β = 60$^{\mathrm{o}}$) the peak axial stress (of 8.3 GPa) occurs shortly after impact at t=2ns, along the edge of the first column and at a depth of 0.15d. Stress wave propagation follows into neighbouring inclined columns via contact from one column to the next, and a complex distribution of dispersive bending waves are established in the array of columns. After t=8ns, the peak axial stress is of magnitude 2.6 GPa at the outer edge of the second column. This resembles the peak state of stress in the vertical array of columns which occurred after t=8ns, recall Fig. 2.

The sensitivity of peak axial stress to the inclination β of vertical columns has also been determined by a series of FE simulations for normal impact. The

nondimensional maximum tensile stress $\bar{\sigma}_a$ in the axial direction is related to the temporal and spatial maximum tensile stress $(\sigma_a)_{max}$ within the columns according to

$$\bar{\sigma}_a = \frac{(\sigma_a)_{max}}{\sqrt{E_{TBC}\rho_{TBC}}V_0} \tag{3}$$

The dependence $\bar{\sigma}_a$ upon β is plotted in Fig. 12a for normal impact. The normalised tensile stress $\bar{\sigma}_a$ increases from 0.32 to a maximum value of 0.96 when β is increased from 30º to 60º, and then decreases to 0.43 in the limit of vertical columns, β=90º. The maximum transient tensile stress $(\sigma_a)_{max}$ occurs within 5ns of impact and at less than 2μm from the top surface of the columns.

4.2 Oblique impact of vertical columns

Recall from Fig. 5 that the peak axial stress within frictionless, vertical columns decreases with increasing angle of obliquity of impact ϕ. Does this conclusion still hold for the case of inclined columns? To investigate this, a limited number of impact simulations have been performed on an array of frictionless columns inclined at β = 60º. Otherwise, the finite element model is the same as that described in the previous section. The observed dependence of $\bar{\sigma}_a$ upon ϕ is plotted is Fig. 12b: as for the case of vertical columns (Fig. 5), the highest axial stresses are generated by normal impact, and drops in an almost symmetric manner with increasing or diminishing ϕ.

5. Concluding remarks

The explicit finite element method has been used to explore the elastodynamic response of the EB-PVD columnar structure to normal and oblique impact by a foreign particle. A complex transient stress pattern emerges from the contact, and contact between the columns can lead to the most intense tensile stresses occurring in columns adjacent to the impacted column. The level of peak axial stress is sufficiently high to induce cracking from the edge of the column and thereby erosion. It is found that the transient tensile stress is sensitive to the size, shape and approach direction of the incoming particle and to the details of the TBC geometry. Moreover, the peak tensile stress is sensitive to the level of friction between columns and between particle and top of TBC coating. This provides a micromechanical explanation for the feature that erosion of TBC coatings is highly stochastic in nature.

References

[1] A.G. Evans, D.R. Mumm, J.W. Hutchinson, G.H. Meier, F.S. Pettit, 'Mechanisms controlling the durability of thermal barrier coatings', Prog. Mater. Sci. 46 [5] 505-553 (2001).

[2] D. D Hass, A.J Slifka and H.N.G Wadley, 'Low thermal conductivity vapour deposited zirconia microstructures', *Acta Mater*., 49 [6] 973-983 (2001).

[3] S. Gu, T.J. Lu, D.D Hass and H.N.G. Wadley, 'Thermal conductivity of zirconia coatings with zig-zag pore microstructures', *Acta Mater*., 49 [13], 2539-2547 (2001).

[4] J.R. Nicholls, M.J. Deakin, and D.S. Rickerby, 'A comparison between the erosion behaviour of thermal spray and electron beam vapour deposition thermal barrier coatings', *Wear* 233, 352-361 (1999).

[5] R.G. Wellman, M.J. Deakin, and J.R. Nicholls, 'The effect of TBC morphology on the erosion rate of EB-PVD TBCs', *Wear* 258 [1-4] 349-356 (2005).

[6] R.G. Wellman, M.J. Deakin, and J.R. Nicholls, 'The effect of TBC morphology and aging on the erosion rate of EB-PVD TBCs', *Tribology International* 38 [9] (2005) 798-804 (2005).

[7] A.G. Evans, N.A. Fleck, S. Faulhaber, N. Vermaak, M. Maloney, and R. Darolia, 'Scaling laws governing the erosion and impact resistance of thermal barrier coatings', *Wear*, 260 [7-8] 886-894 (2006).

[8] X. Chen, M.Y. He, I. Spitsberg, N.A. Fleck, J.W. Hutchinson, and A.G. Evans, 'Mechanisms governing the high temperature erosion of thermal barrier coatings', *Wear*, 256 [7-8] 735-746 (2004).

[9] Th. Zisis, and N.A. Fleck, ‘Mechanisms of elastodynamic erosion of electron-beam thermal barrier coatings’, *Int. J. Mat. Res*., 98 [12] 1196-1202, (2007).

[10] N.A. Fleck and Th Zisis, ‘The erosion of EB-PVD thermal barrier coatings: the competition between mechanisms, *Wear*, 268 [11-12] 1214-1224 (2010).

[11] R.G. Wellman, and J.R. Nicholls, ‘Some observations on erosion mechanisms of EB PVD TBCs’, *Wear* 242 [1-2] 89-96 (2000).

[12] ABAQUS version 6.5 User’s Manual Hibbitt, Karlsson and Sorensen Inc.

[13] K.L. Johnson, *Contact Mechanics*, Cambridge Press, (1985).

[14] H. Tada, P. Paris, and G. Irwin, *The Stress Analysis of Cracks Handbook*, Del Research Corporation, (1973).

Figure captions

Figure 1. Impact of vertical TBC columns, resting upon a rigid substrate.
(a) plane strain case, circular cylindrical particle obliquely impacting an array of rectangular strips; (b) axisymmetric case, normal impact of a concentric array of annuli by a spherical particle.

Figure 2. Time sequences of axial tensile stress for normal impact $\phi = 0$ and inclined impact at $\phi = 45^{o}$. The white zone denotes compression.

Figure 3. The peak tensile stress $\overline{\sigma}_{22}$ versus *d/R* for selected initial velocities. (a) plane strain case, (b) axisymmetric case.

Figure 4. The column number *n* for which the tensile axial stress has a global and temporal maximum value versus *d/R*. (a) plane strain and (b) axisymmetric case.

Figure 5. Peak stress $\overline{\sigma}_{22}$ versus impact angle ϕ for selected impact locations.

Figure 6. The axial stress distribution at the instant of maximum spatial and temporal axial component $(\sigma_{22})_{max}$. (a) at time t=7ns, for normal impact with frictionless conditions, (b) t=3.5ns, under normal impact with $\mu_S=\mu_C=1$, (c) t=8ns under oblique impact ϕ=45º with frictionless conditions, and (d) t=14.5ns under oblique impact ϕ=45º with $\mu_S=\mu_C=1$.

Figure 7. Oblique impact by an angular particle.

Figure 8. Nondimensional tensile stress $\overline{\sigma}_{22}$ versus impact angle for the circular particle, and square particle with ψ=0 and initial location s=0. (a) $\mu_s=\mu_c=0$ and (b) $\mu_s=\mu_c=1$.

Figure 9. Nondimensional tensile stress $\overline{\sigma}_{22}$ versus impact angle for frictionless impact by the square particle. (a) impact locations s=0, 0.25d and -0.25d, with ψ=0; (b) initial location s=0 but particle orientated at ψ=-π/8, 0, π/8 and π/4.

Figure 10. Sketch of the plane strain model for the normal impact of inclined columns.

Figure 11 Typical response of inclined columns, inclined at β=60^o, showing the axial tensile stress following normal impact. The white colour denotes a state of compression.

Figure 12 (a) Peak axial stress versus inclination of the columns β for nomal impact ϕ=0; (b) peak axial stress versus impact angle ϕ for β=75^o.

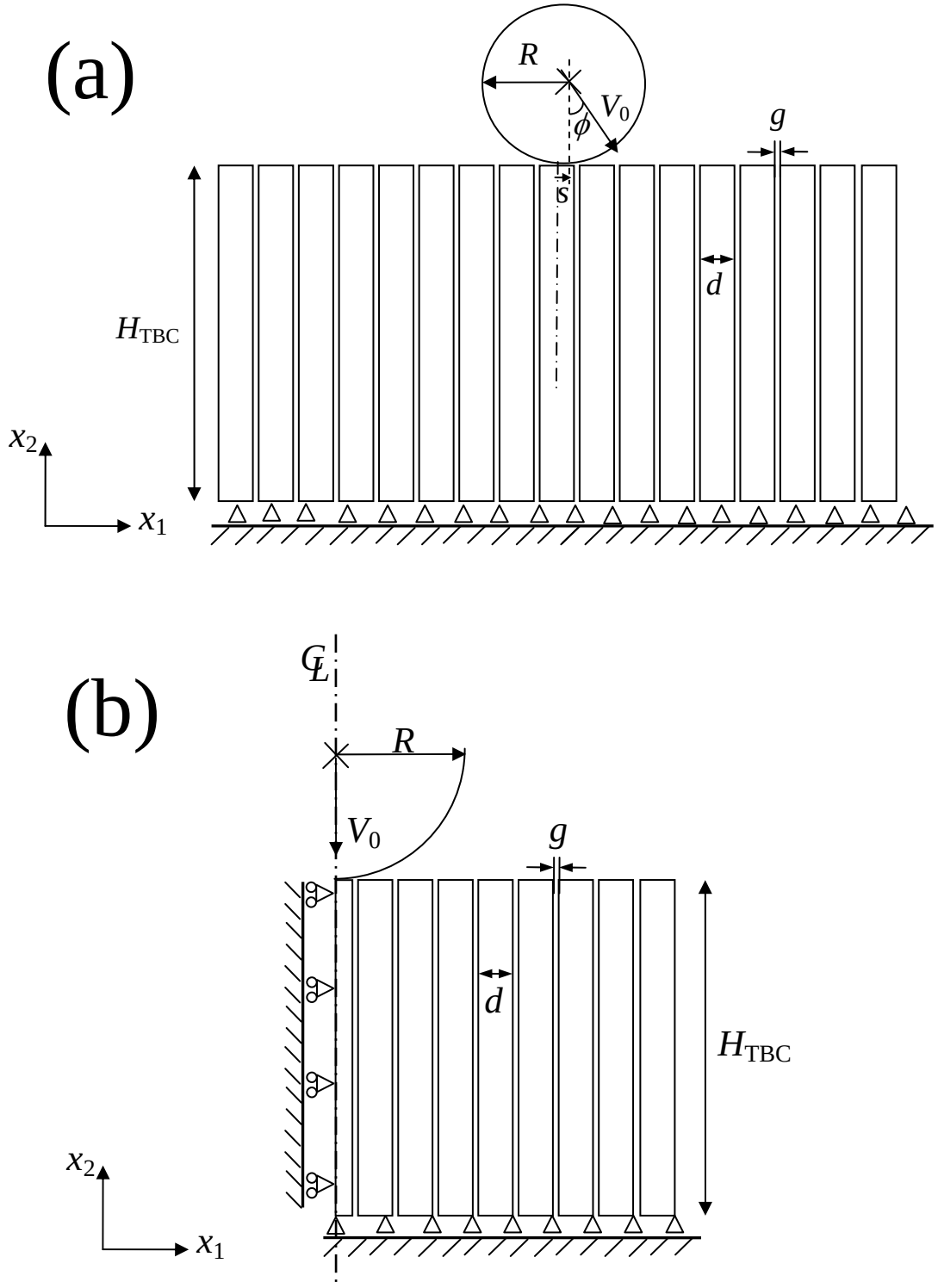

Figure 1. Impact of vertical TBC columns, resting upon a rigid substrate.
(a) plane strain case, circular cylindrical particle obliquely impacting an array of rectangular strips; (b) axisymmetric case, normal impact of a concentric array of annuli by a spherical particle.

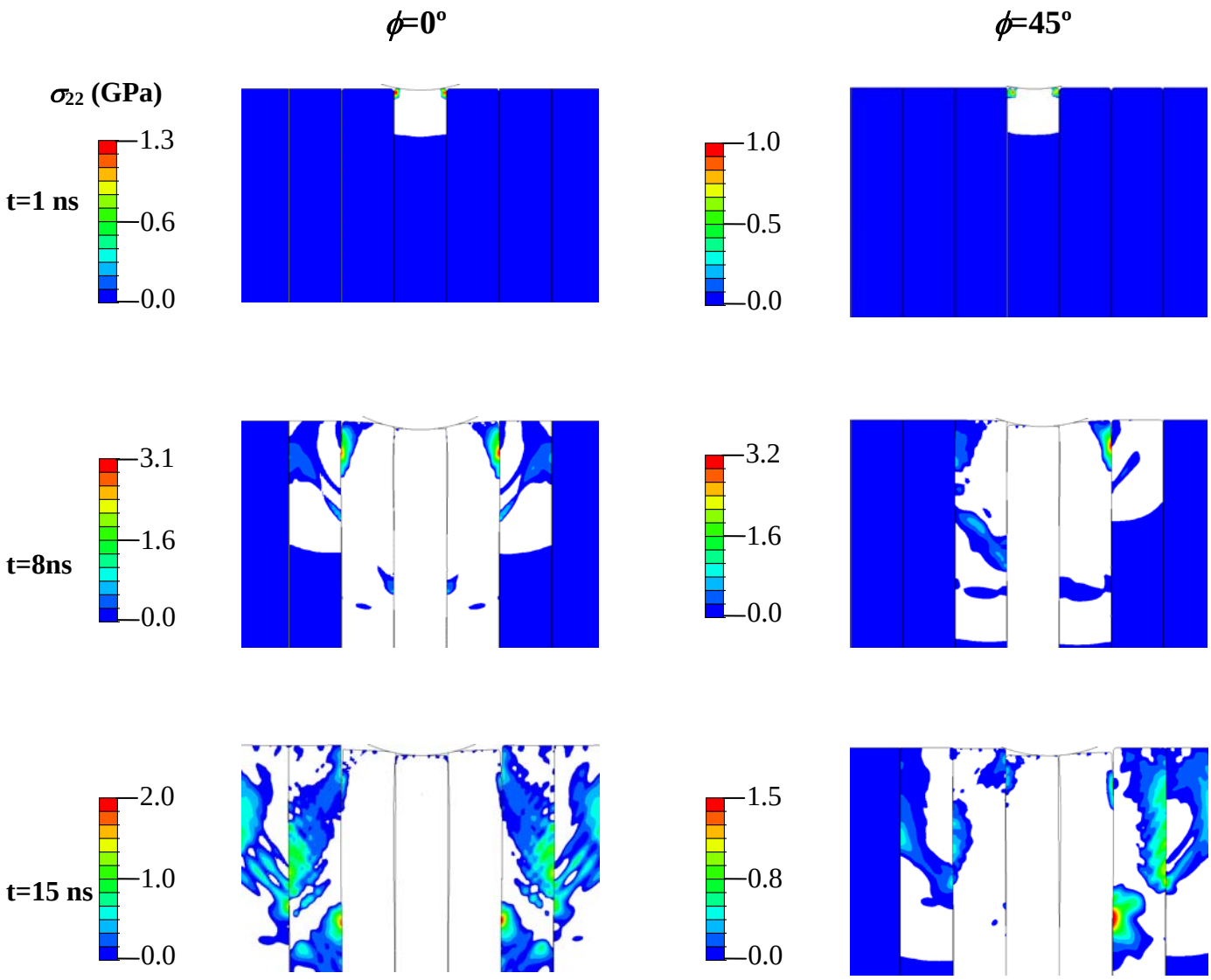

Figure 2. Time sequences of axial tensile stress for normal impact $\phi = 0$ and inclined impact at $\phi = 45^{o}$. The white zone denotes compression.

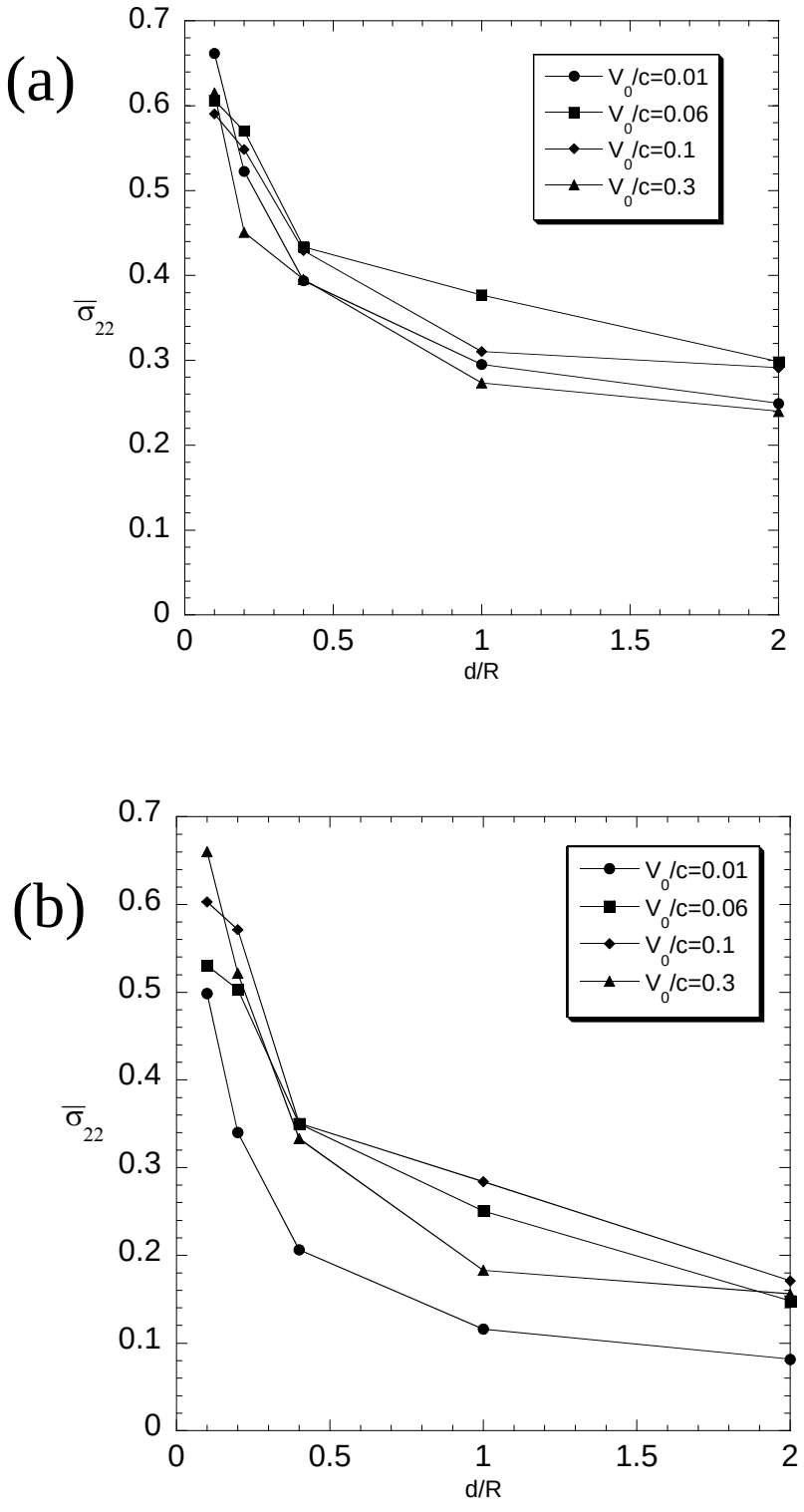

Figure 3. The peak tensile stress $\overline{\sigma}_{22}$ versus *d/R* for selected initial velocities. (a) plane strain case, (b) axisymmetric case.

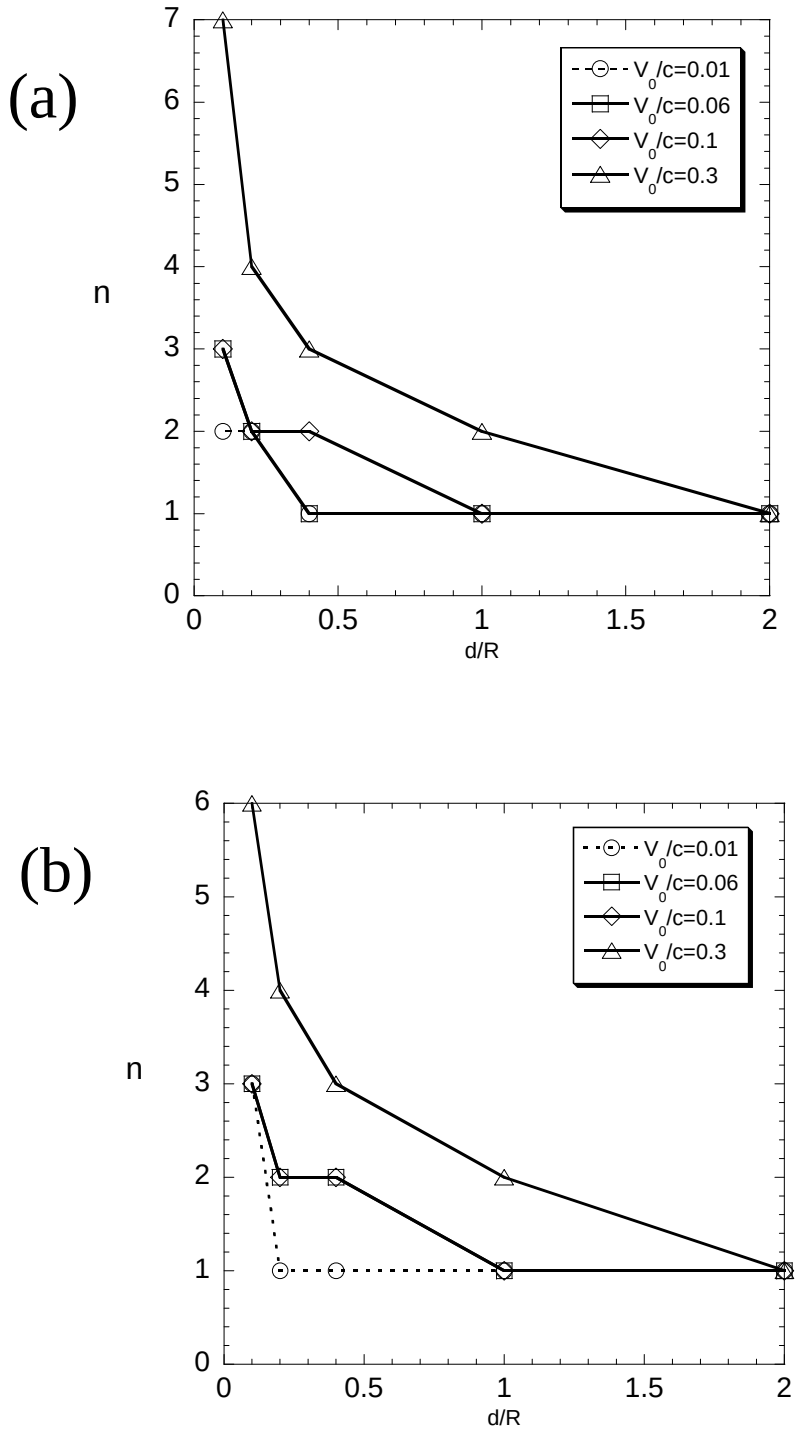

Figure 4. The column number *n* for which the tensile axial stress has a global and temporal maximum value versus *d/R*. (a) plane strain and (b) axisymmetric case.

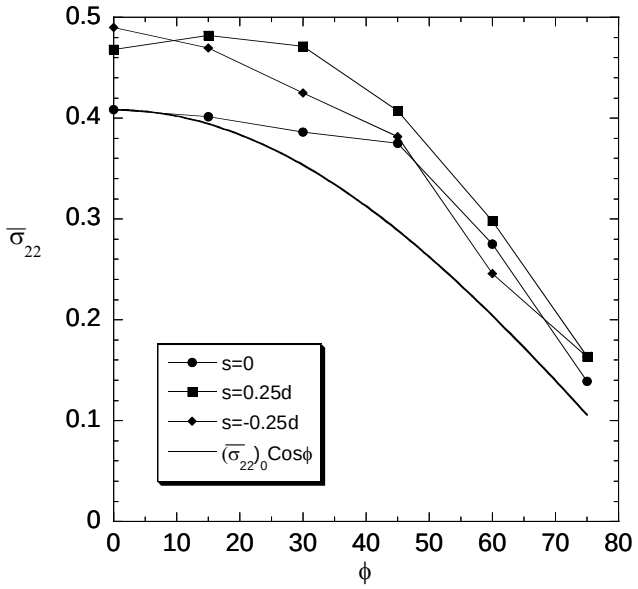

Figure 5. Peak stress $\overline{\sigma}_{22}$ versus impact angle ϕ for selected impact locations.

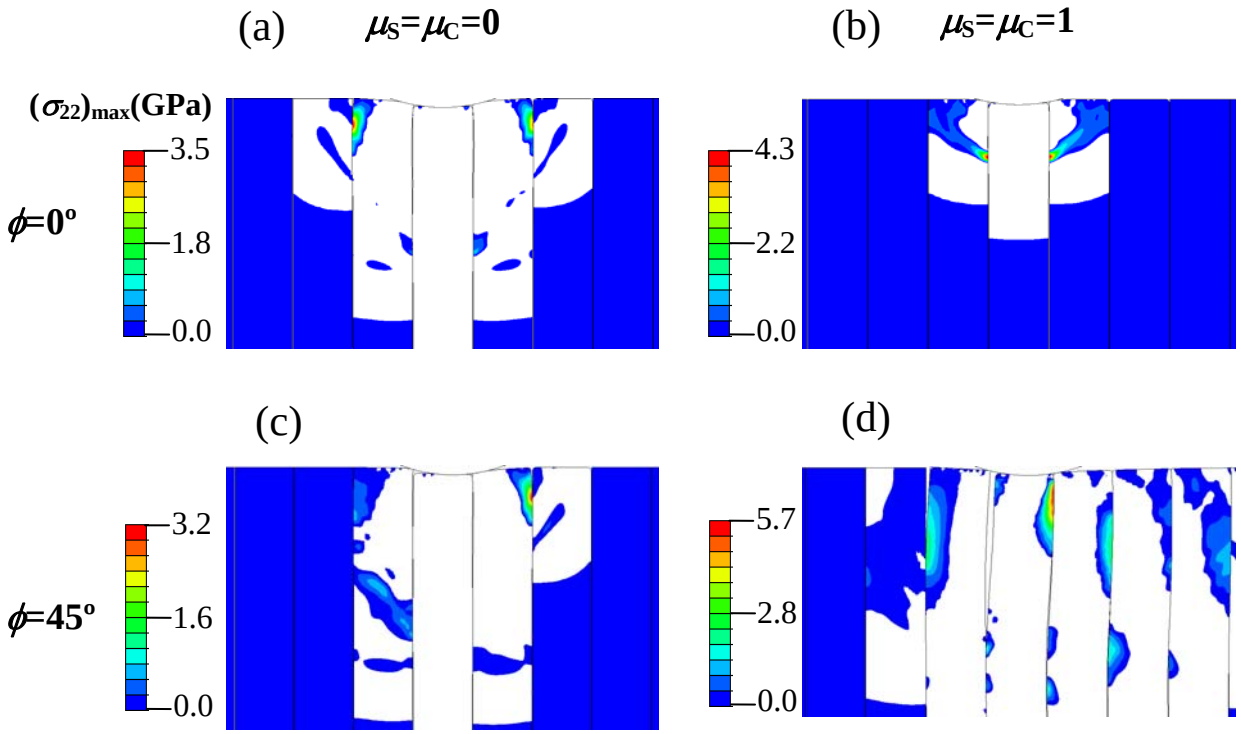

Figure 6. The axial stress distribution at the instant of maximum spatial and temporal axial component $(\sigma_{22})_{max}$. (a) at time t=7ns, for normal impact with frictionless conditions, (b) t=3.5ns, under normal impact with $\mu_S=\mu_C=1$, (c) t=8ns under oblique impact ϕ=45° with frictionless conditions, and (d) t=14.5ns under oblique impact ϕ=45° with $\mu_S=\mu_C=1$.

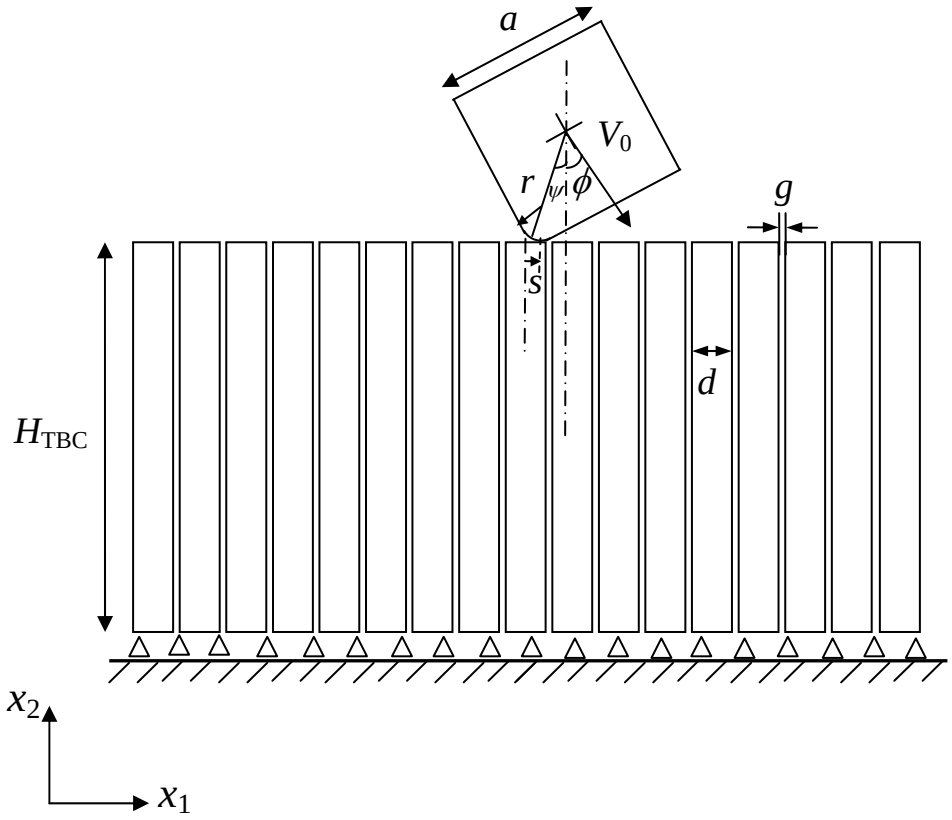

Figure 7. Oblique impact by an angular particle.

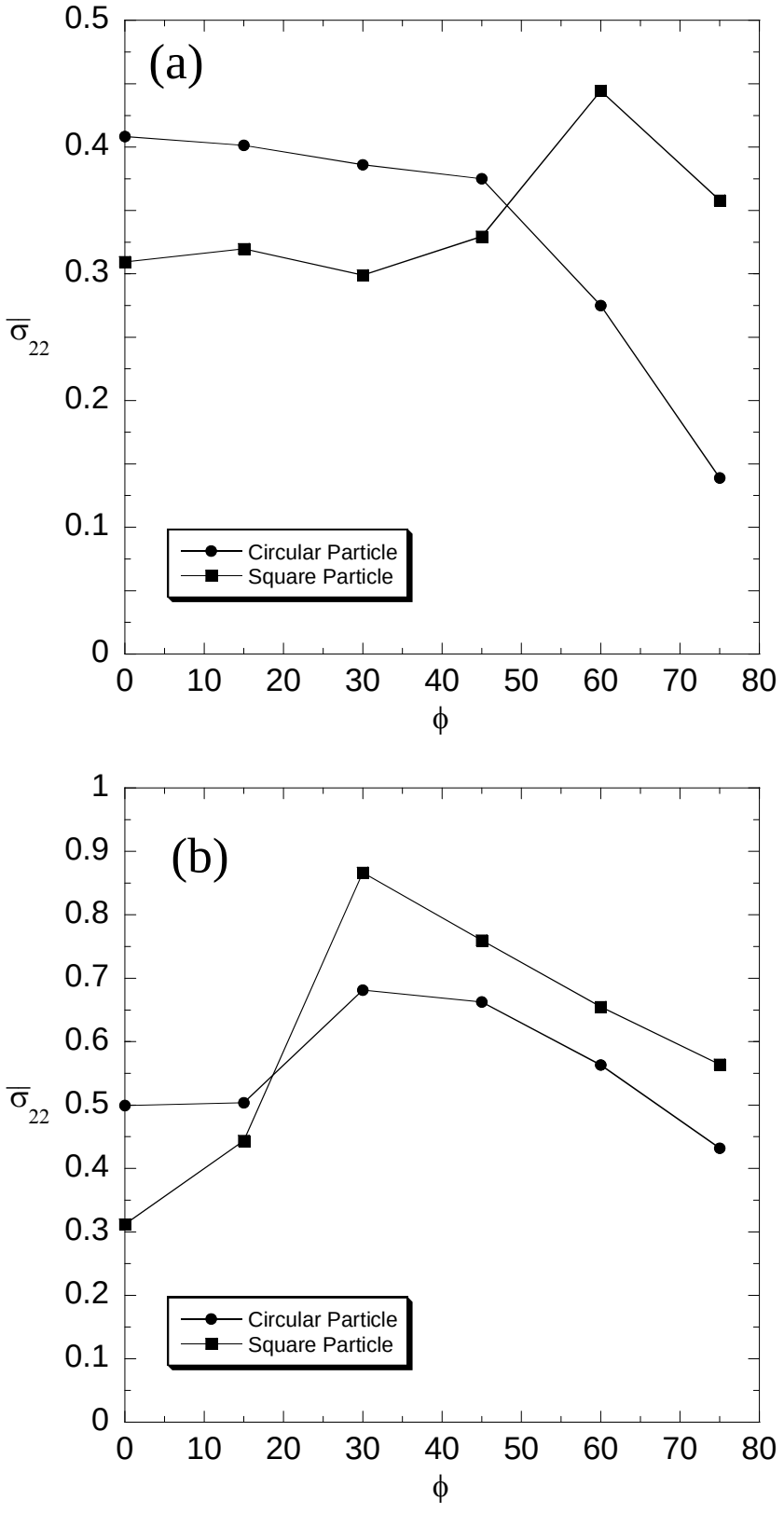

Figure 8. Nondimensional tensile stress $\overline{\sigma}_{22}$ versus impact angle for the circular particle, and square particle with ψ=0 and initial location s=0. (a) $\mu_s=\mu_c=0$ and (b) $\mu_s=\mu_c=1$.

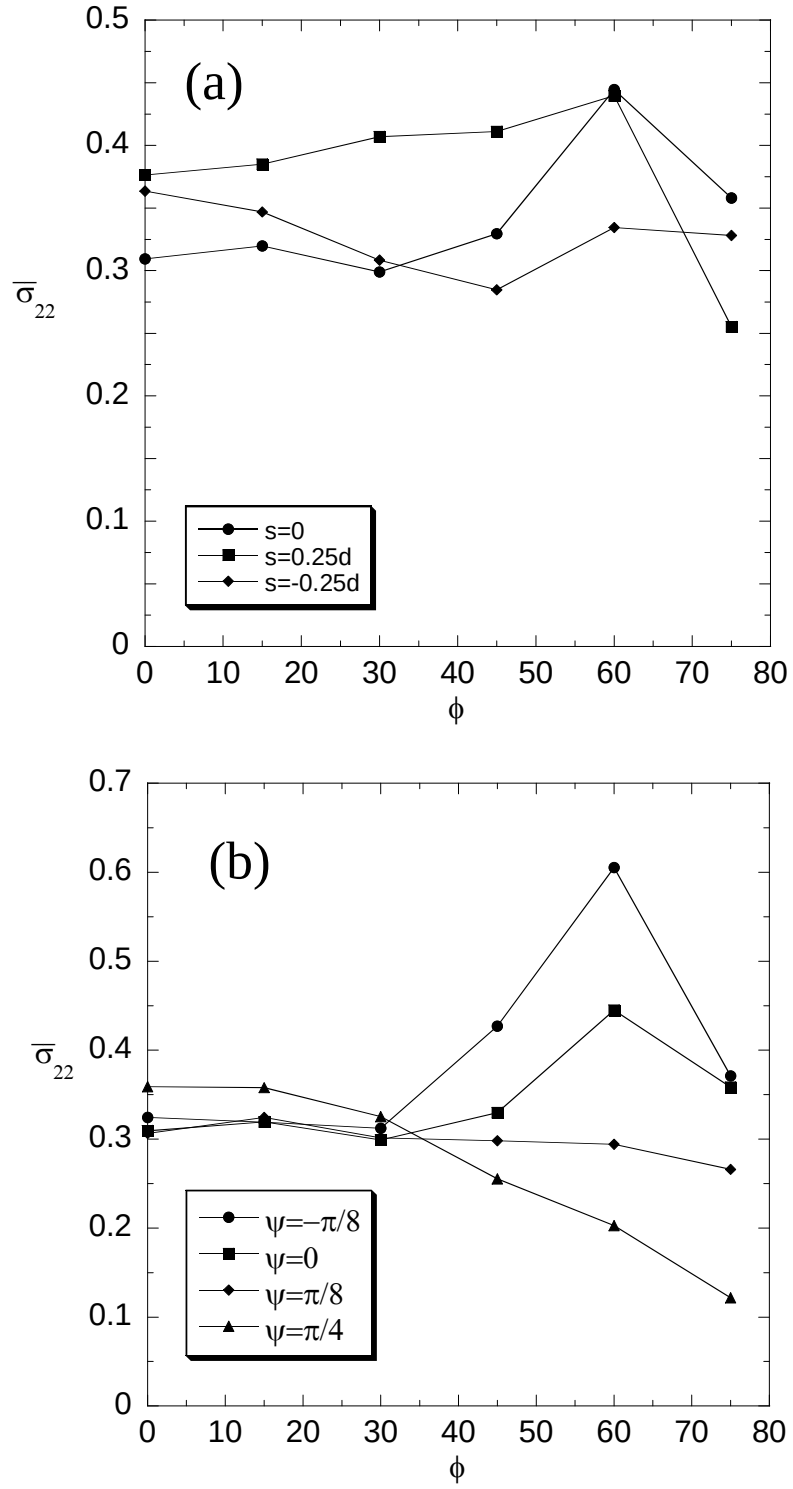

Figure 9. Nondimensional tensile stress $\overline{\sigma}_{22}$ versus impact angle for frictionless impact by the square particle. (a) impact locations s=0, 0.25d and -0.25d, with ψ=0; (b) initial location s=0 but particle orientated at ψ=-π/8, 0, π/8 and π/4.

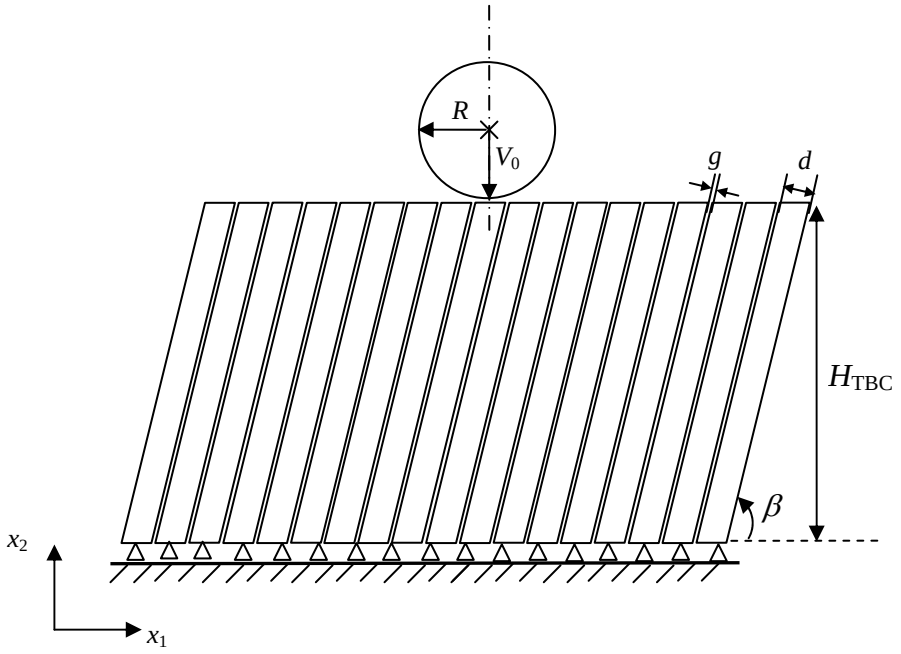

Figure 10. Sketch of the plane strain model for the normal impact of inclined columns.

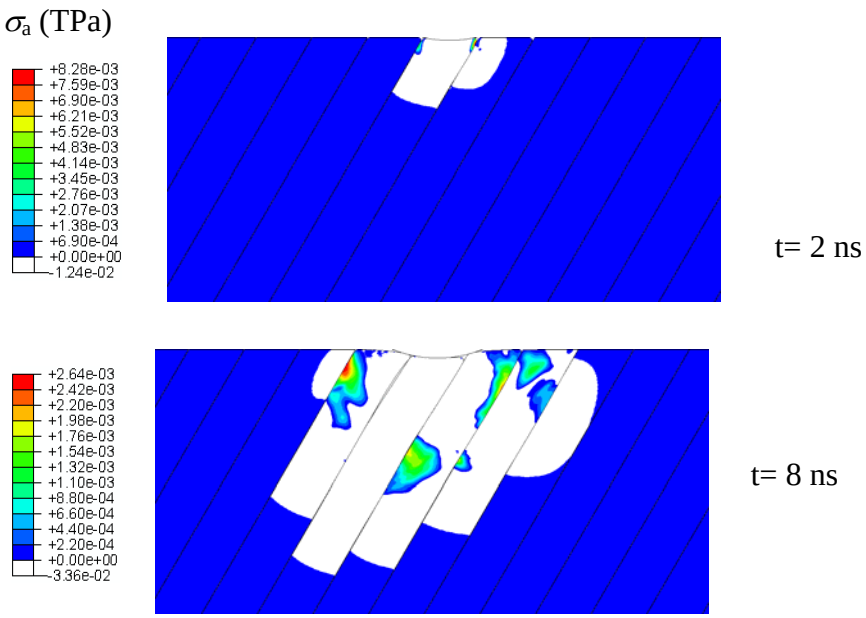

Figure 11 Typical response of inclined columns, inclined at β=60^o, showing the axial tensile stress following normal impact. The white colour denotes a state of compression.

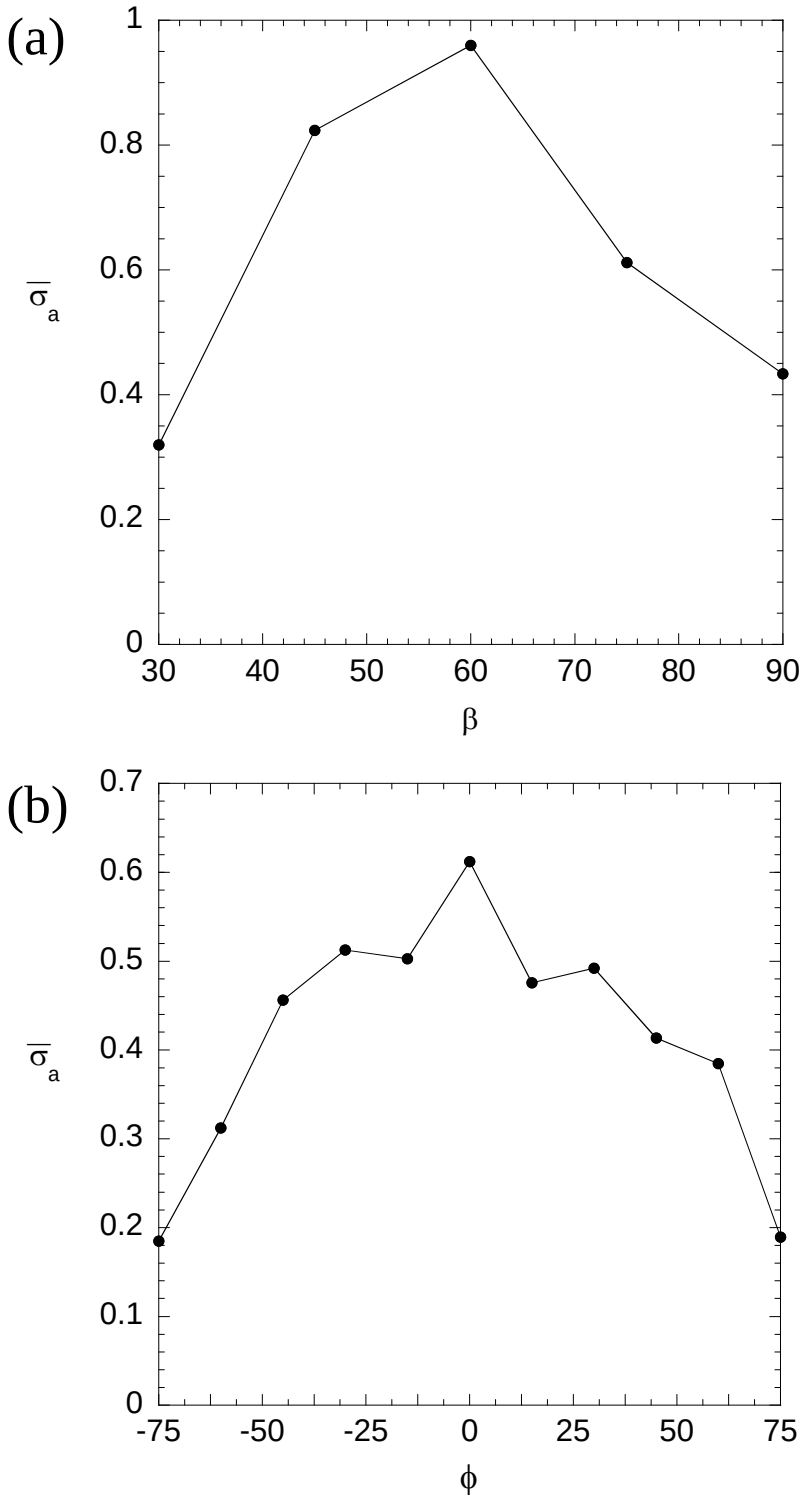

Figure 12 (a) Peak axial stress versus inclination of the columns β for nomal impact ϕ=0; (b) peak axial stress versus impact angle ϕ for β=75^o.